

THE OFFICIAL MAGAZINE OF THE OCEANOGRAPHY SOCIETY

Oceanography

CITATION

Johnston, T.M.S., D. Chaudhuri, M. Mathur, D.L. Rudnick, D. Sengupta, H.L. Simmons, A. Tandon, and R. Venkatesan. 2016. Decay mechanisms of near-inertial mixed layer oscillations in the Bay of Bengal. *Oceanography* 29(2):180–191, <http://dx.doi.org/10.5670/oceanog.2016.50>.

DOI

<http://dx.doi.org/10.5670/oceanog.2016.50>

COPYRIGHT

This article has been published in *Oceanography*, Volume 29, Number 2, a quarterly journal of The Oceanography Society. Copyright 2016 by The Oceanography Society. All rights reserved.

USAGE

Permission is granted to copy this article for use in teaching and research. Republication, systematic reproduction, or collective redistribution of any portion of this article by photocopy machine, reposting, or other means is permitted only with the approval of The Oceanography Society. Send all correspondence to: info@tos.org or The Oceanography Society, PO Box 1931, Rockville, MD 20849-1931, USA.

Decay Mechanisms of Near-Inertial Mixed Layer Oscillations in the Bay of Bengal

By T.M. Shaun Johnston, Dipanjan Chaudhuri,
Manikandan Mathur, Daniel L. Rudnick, Debasis Sengupta,
Harper L. Simmons, Amit Tandon, and R. Venkatesan

ABSTRACT. Winds generate inertial and near-inertial currents in the upper ocean. These currents dominate the kinetic energy and contain most of the vertical shear in horizontal currents. Subsequent shear instabilities lead to mixing. In the Bay of Bengal, the annual mean wind energy input and near-inertial mixed layer energy is almost as large as in the mid-latitude storm tracks. Also, mixing associated with these waves is known to affect mixed layer heat content, sea surface temperature, and, thus, precipitation in coupled global models. Therefore, the mechanisms leading to the decay of these currents in the mixed layer and below are of considerable importance. Two such decay mechanisms are examined here. One mechanism is the downward propagation of near-inertial internal waves, which is aided by the mesoscale circulation and is observed with a rapidly profiling float. In a few days (faster than at mid-latitudes), the near-inertial wave group propagated from the base of the mixed layer to 250 m depth in the stratified interior. Another decay mechanism is enhanced shear generation at the mixed layer base from periodic alignment of rotating, near-inertial current shear and winds, which is observed with a mooring and analyzed with a simple two-layer model.

INTRODUCTION

Importance of Near-Inertial Internal Waves

Steady surface winds produce frictional transport to the right of the wind in the Northern Hemisphere, while an impulsive change in wind speed or direction excites oscillations at the local inertial period in the surface mixed layer (ML; Ekman, 1905). Steady winds produce vertical shear in horizontal currents (shear, hereafter) at the base of the ML and subsequently deepen the ML via mechanical mixing. However, with inertially rotating winds, the similarly rotating currents can propagate into the oceanic interior without much effect on ML depth (MLD; Dohan and Davis, 2011). Also, unidirectional winds with fluctuating magnitude excite such inertial motions (Weller et al., 2014; Majumder et al., 2015), which may have greater effects in the northern Bay of Bengal (BoB) due to its thin ML (Wijesekera et al., in press). The inertial currents heave the base of the ML to produce propagating near-inertial internal waves (NIWs) in the stratified ocean (Simmons and Alford, 2012). Long-wavelength NIWs may propagate horizontally far from their source regions, while short-wavelength NIWs propagate vertically and may contribute to local mixing when shear overcomes the buoyancy restoring force in stratified waters or when strain (vertical stretching apart of isopycnals) reduces the stratification (Hebert and Moum, 1994; Alford and Gregg, 2001). Inertial and near-inertial currents often dominate the kinetic energy and contain most of the current shear (Alford et al., 2016). Thus, where and how this episodic near-inertial energy dissipates affects not only the upper ocean but the stratified interior as well. When global coupled atmosphere-ocean models include NIW-driven mixing, substantial changes occur in the MLD, tropical sea surface temperature, and precipitation (Jochum et al., 2013).

The mechanisms leading to the decay

of near-inertial ML currents have been of much interest in the last 30 years. Simmons and Alford (2012) discuss NIW generation and the propagation of the longest wavelengths, while Alford et al. (2016) review a broad range of topics and open questions, including the uncertain fate of short-wavelength NIWs. Our observations and analyses (a) show that groups of short-wavelength NIWs propagate rapidly into the interior and can remove energy from ML inertial oscillations; (b) suggest that mesoscale circulation aids the rapid downward propagation of short-wavelength NIWs; and (c) indicate that alignment of near-inertial current shear and wind leads to spikes in shear generation and presumably mixing and energy extraction from the ML.

Formation and Propagation of Near-Inertial Internal Waves

The classical mechanism for the generation and evolution of near-inertial motions can be explained by considering the response to a rapid increase in wind forcing on a horizontally uniform ocean. After the onset of winds, ML inertial oscillations begin. Due to Earth's rotation, the near-inertial velocity rotates clockwise in time in the Northern Hemisphere at the Coriolis frequency $f = 2\pi/T_i = 2\Omega \sin \theta$, where the inertial period is T_i ($= 43\text{--}39$ hours from 16°N – 18°N in our study area), Earth's rotation rate is Ω , and the latitude is θ (Ekman, 1905). Under broad storms in mid-latitudes with length scales reaching 1,000 km, flow converges because the inertial period changes with latitude (D'Asaro et al., 1995), which is referred to as the β effect. As the ML inertial currents converge/diverge, the base of the ML heaves downward/upward, which in turn produces heaving of isopycnals in the stratified interior and generates NIWs there (Gill, 1984). This process explains how long-wavelength NIWs are generated, which propagate far from their source regions, carry much of the

energy, and are well reproduced by models (Simmons and Alford, 2012).

The small-scale structure, however, is not well described by this approach based on oceanic vertical normal modes (Gill, 1984; D'Asaro et al., 1995). These vertical modes arise from considering that vertical displacement of fluid particles in the water column is fixed to zero at the surface and bottom. Therefore, only certain wavelengths can be excited depending on the stratification and height of the water column in a finite depth ocean. This construction is analogous to the notes generated on a plucked string on a musical instrument. Alternatively, the propagation of NIWs in a field of mesoscale, geostrophic eddies can be treated as an initial value problem (Young and Ben Jelloul, 1997). The local rotation of the flow in the vicinity of strong fronts and eddies in Earth's rotating frame, also known as the relative vorticity, can be comparable in magnitude to the planetary vorticity (or rotation denoted by f as described in the previous paragraph). Both the relative vorticity associated with the mesoscale eddies and the change in planetary vorticity with latitude (β effect) can enhance the vertical transmission of near-inertial energy out of the ML (D'Asaro et al., 1995; Young and Ben Jelloul, 1997).

In this contribution, we focus on short-wavelength NIWs, which propagate vertically, display greater current shear in the vertical, and can contribute to local mixing. In the interior, typical NIWs have frequencies of $1\text{--}1.2 f$, vertical wavelengths of 100–400 m, and horizontal wavelengths of order 10–100 km (Alford et al., 2016). In contrast, the lowest modes or longest waves have vertical wavelengths of twice the ocean depth and horizontal wavelengths of hundreds of kilometers. Typical vertical propagation at mid-latitudes is about 10 m day^{-1} (Alford et al., 2016). The downward group velocity is much faster in some of our observations in the BoB, which may be due to active mesoscale circulation.

Near-Inertial Internal Waves in the Bay of Bengal

The Ocean Mixing and Monsoon (OMM) program of India's National Monsoon Mission in the Ministry of Earth Sciences and the Air-Sea Interactions Regional Initiative (ASIRI) of the US Office of Naval Research catalyze a large collaboration between Indian and US scientists. The aims are to understand small-scale processes affecting air-sea interaction in the BoB, to ultimately improve monsoon prediction on hourly to subseasonal time scales (Goswami et al., 2016, in this issue), and to train the next generation of scientists and build capacity (Tandon et al., 2016, in this issue). Climate models of the BoB are biased compared to observations, producing cold sea surface temperatures and deeper MLs (Fousiya et al., 2015; Parekh et al., 2015; Chowdary et al., 2016a), perhaps due to negative biases in surface heat flux (Chowdary et al., 2016a). Also, unrealistically weak biases in stratification allow stronger mixing, which, in turn, allow deep biases in MLD and cold biases in sea surface temperature (Fousiya et al., 2015; Parekh et al., 2015; Chowdary et al., 2016b, in this issue). These biases may be due to a lack of restratification by prevalent but unresolved submesoscale features in the BoB (Ferrari and Boccaletti, 2004; MacKinnon et al., 2016, in this issue).

In another coupled global model, NIW-related mixing improves tropical sea surface temperature and precipitation (Jochum et al., 2013). In the models mentioned above, we speculate that such mixing might exacerbate the biases and produce still deeper MLs and colder sea surface temperatures. On the other hand, we speculate further that if considerable near-inertial energy propagates quickly into the interior in the BoB, the biases could be reduced. The questions of what fraction of the ML near-inertial oscillations contributes to local mixing and what fraction propagates away as NIWs into the ocean interior are, therefore, important for coupled global models (Jochum et al., 2013). How does NIW

generation in the BoB compare with that of mid-latitudes? At mid-latitudes, inertially rotating winds force inertial rotation in the ocean. In the BoB, winds can be unidirectional (see later discussion), but NIWs can also be generated by changing wind magnitude rather than inertial rotation (Weller et al., 2014; Majumder et al., 2015). The annual mean wind work and the near-inertial ML energy are almost as large in the BoB as in mid-latitude storm tracks (Chaigneau et al., 2008; Simmons and Alford, 2012). In mid-latitudes, MLs are deeper in winter and thus will project on longer vertical wavelengths, as observed by D'Asaro et al. (1995). Short-wavelength NIWs are expected in the BoB due to shallower MLs.

As noted above, decay of ML near-inertial motions and short-wavelength NIW propagation are not well understood in realistic ocean settings. Further complexity comes from the horizontal and vertical structure of the upper ocean in the BoB (Gordon et al., Hormann et al., MacKinnon et al., Sarkar et al., Shroyer et al., and Thangaprakash et al., 2016, all in this issue). For example, enhanced vertical fluxes are noted at fronts in the BoB and elsewhere (Johnston et al., 2011; Lucas et al., 2016, in this issue). In the BoB, the ML is thin (~10 m) and controlled by freshwater input from major river systems and precipitation (Figure 1; Goswami et al., and Gordon et al., 2016, both in this issue). Further below, a stratification maximum at ~50 m depth lies over the weakly stratified, deep, interior ocean. This transition layer between the ML and stratified interior mediates fluxes from the surface to the interior (Johnston and Rudnick, 2009; Dohan and Davis, 2011; Majumder et al., 2015) and inhibits vertical fluxes in the BoB (Lucas et al., and Sarma et al., 2016, both in this issue). If shear (S) is comparable to stratification (commonly measured with the frequency of vertical oscillations in a stratified fluid or the buoyancy frequency, N), then mixing is possible when their squared ratio or Richardson number, denoted $Ri = N^2/S^2$, is less than

0.25. Ri is often order one in the transition layer, suggestive of instability. Both pre-existing shear from remotely generated NIWs in the transition layer and downward propagation of locally generated NIWs contribute to the near-inertial ML energy budget (Plueddemann and Farrar, 2006). Wind and near-inertial shear alignment is important for shear generation, subsequent mixing, and, thus, the ML energy budget (Brannigan et al., 2013; Majumder et al., 2015).

Mesoscale Effects on Vertical Energy Propagation

NIW vertical energy flux depends on the product of the energy density of the waves and their vertical group speed, $c_{gz} \approx N^2 \alpha^3 \lambda_x / (2\pi\omega)$, where the aspect ratio of vertical to horizontal wavelengths is $\alpha = \lambda_z / \lambda_x$ and the wave's radial frequency is ω (Gill, 1982). The aspect ratio depends sensitively on the difference between wave frequency and inertial frequency. The horizontal length scales of ML inertial motions are imposed by atmospheric forcing, which has a length scale of order 1,000 km. To reduce their horizontal wavelength or horizontal coherence, oceanic inertial motions in the ML must be disrupted to allow vertical propagation into the interior (D'Asaro et al., 1995). The β effect explains the decay of surface drifters' inertial motions (Park et al., 2009), but neither observations of the predicted rapid decay e -folding scale of less than four days equatorward of ~20°N nor subsurface data are noted in Park et al. (2009).

Eddies can influence vertical propagation in at least five ways. (While we discuss eddies in this paragraph, identical processes occur at fronts, current jets, or other meso- and submesoscale features.) (1) They may bring stratified water closer to the base of the ML. (2) A key feature is their relative vorticity or, in other words, the local rotation of a fluid parcel (Weller, 1982; Kunze, 1985). The vertical component of eddy vorticity can either be in the same (counterclockwise, positive, cyclonic) or opposite

(clockwise, negative, anticyclonic) direction of Earth's rotation. Thus, the effective inertial frequency decreases when the eddies rotate clockwise, which in turn increases the aspect ratio of the waves and increases their vertical group speed. Internal waves may also become trapped in regions of negative vorticity. (3) As the mesoscale flow converges, the rotational radius of near-inertial motions decreases. Also, the near-inertial current amplitude then increases to conserve angular momentum (Weller, 1982). As the radius/wavelength of near-inertial motions decreases, vertical group speed increases. (4) As near-inertial motions encounter a field of mesoscale eddies of smaller length scale, the near-inertial motions sample a number of eddies and lose coherence proportional to the kinetic energy in the spatially varying flow field (Young and Ben Jelloul, 1997). This process reduces the length scale of the near-inertial motions. (5) The shear of the background currents causes internal waves to refract and reduce their vertical wavelengths (Kunze, 1985). When the waves' propagation speed is equal and opposite to the current speed, a critical level is reached, at which the energy cannot propagate vertically any further, and the wave breaks (Munk, 1981).

In summary, the vertical group speed can be increased by: (1) reducing horizontal wavelength from mesoscale currents dephasing inertial motions (Young and Ben Jelloul, 1997), from flow convergence (Weller, 1982), or from the stronger β effect (D'Asaro et al., 1995; Park et al., 2009); and (2) lowering the effective inertial frequency due to the relative vorticity of anticyclones or clockwise eddies and making the NIWs effectively more superinertial (Weller, 1982; Kunze, 1985; Elipot et al., 2010). Also, vertical propagation can be augmented at fronts or eddies, where stratified water is brought closer to the ML. In anticyclones, internal waves may become trapped and amplified (Munk, 1981; Kunze, 1985).

METHODS

Mooring

The National Institute of Ocean Technology (NIOT, Chennai, India) runs the Ocean Moored Buoy Network for the Northern Indian Ocean (OMNI), which was set up to investigate the strong coupling between monsoons and cyclones within the northern BoB (Venkatesan et al., 2013). The program has deployed moorings with meteorological and subsurface sensors at six different locations in the BoB. Here, we present an analysis of the data at hourly resolution acquired from August to September 2013 at mooring BD09, located at 17.88°N, 89.67°E (Figure 1a). The meteorological sensors are at 3 m above sea level and measure

air temperature, surface pressure, relative humidity, downwelling long- and shortwave radiation, and wind speed and direction. Subsurface conductivity and temperature sensors are at 10 different depths: 5, 10, 15, 20, 30, 50, 75, 100, 200, and 500 m. The mooring also includes one current meter at 1.2 m depth and one downward-looking acoustic Doppler current profiler (ADCP) at 7.5 m, which measures ocean current from 10–105 m at 5 m resolution.

Float

A SOLO-II profiling float (serial number 8119; Argo platform number 5904302) was deployed at a front near 16.5°N, 85.5°E in the BoB in conjunction with

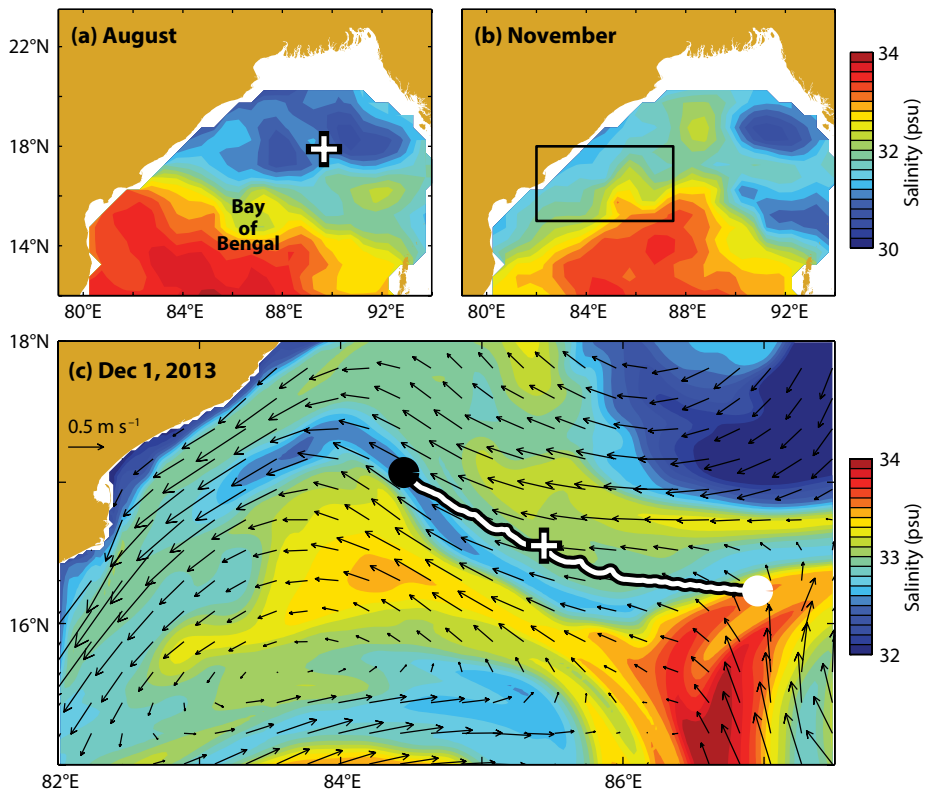


FIGURE 1. Sea surface salinity from the Argo climatology shows (a) large freshwater input to the northern part of the Bay of Bengal in August, and (b) extension of the freshwater down the boundaries of the bay in November. The position of mooring BD09 of the Ocean Moored Buoy Network for the Northern Indian Ocean (OMNI) program is indicated with a plus sign in (a). The broad picture from Argo is complemented by model results on December 1, 2013, averaged over the upper 23 m, which shows (c) freshwater and salty water strained into narrow filaments by cyclonic (counterclockwise) and anticyclonic (clockwise) eddies south and north of the float trajectory (line). The float was released on November 21, 2013 (white circle), at the front and completed rapid profiling on December 7, 2013 (black circle). The position of the float is indicated on December 1, 2013, by a plus sign. Current vectors are lowpassed beyond three days using wavelets. A scale vector of 0.5 m s⁻¹ is plotted in the upper left.

ship surveys by R/V *Roger Revelle* in 2013 (Figure 1c). The float profiled from 0–250 m and back every 1.7 hours. After completing 237 profiles, the float entered the typical Argo mode with a profile every 10 days, which does not resolve the inertial frequency. The rapid profiling lasted from November 21 to December 7, 2013.

The float has a pumped Sea-Bird Electronics (SBE) 41CP conductivity-temperature-depth (CTD) instrument from which potential temperature (θ), salinity (S), in situ density (ρ), and potential density (σ_θ) are obtained on ascents, when the CTD encounters clean flow. Float data are averaged in 10 m bins from 10–250 m depth. The float moves upward by inflating an external bladder to gain buoyancy. Downward motion is achieved by shifting mineral oil back into the pressure case and thereby deflating the bladder and decreasing the vehicle's buoyancy (Davis et al., 2001). A float is assumed to drift with the current, and the depth-mean current over a dive cycle is obtained from GPS fixes at consecutive surface intervals.

Signals with frequencies higher than the profiling frequency are smeared and aliased and cannot be subsequently disentangled. Due to its slow motion of ~ 20 km day⁻¹, the drifting float smears this high-frequency temporal variability into spatial variability (Figure 1c; Rudnick and Cole, 2011). Aliasing arises because the profiling frequency is in the internal wave band. By using the analysis method described below, the effects of smearing and aliasing on near-inertial motions are mitigated.

For analysis of NIWs, the data from a slowly moving platform are analyzed as slowly moving time series (Johnston et al., 2015). Since the platform is moving and NIWs are episodic, the expected signal is well suited to a wavelet analysis, which resolves variance as functions of time and wave period. The analysis is done by convolving the time series with a wavelet, a compact function in time and frequency. (Note the contrast with Fourier spectral analysis using sine

waves, which may produce precise frequency lines, but has no resolution in time.) To analyze the expected signal of NIW groups, we use the Morlet wavelet, which has a similar character—namely, a sinusoidal oscillation within a Gaussian envelope. Our averaging window for inertial motions is determined from this envelope, which has a full width at the e -folding level of $2\sqrt{T_i}$ or about five days. Near-inertial and semidiurnal motions are band passed within $\pm 25\%$ of the central frequency using wavelets. Mesoscale motions are obtained from the float via a three-day low-pass filter using wavelets. Since NIWs have flat aspect ratios (long horizontal and short vertical wavelengths), they are better detected with velocity rather than in isopycnal displacements. However, both shear (vertical gradient of horizontal currents) and strain (vertical gradient of isopycnal displacements) are implicated in mixing (Alford and Gregg, 2001). The float does not measure depth-dependent currents and so to obtain information on the vertical propagation of NIWs, we use the band-passed potential density fluctuations.

To help understand the in situ float data, surface winds are obtained from a global data assimilation by the National Center for Environmental Prediction (Kalnay et al., 1996).

Model

We use the Regional Ocean Modeling System (ROMS) to understand the sub-mesoscale and mesoscale structure during the float mission (Figure 1c). To allow the model to evolve freely, it was initialized and given lateral boundary conditions from an oceanic state estimate and run with a reanalysis atmospheric state and a prognostic ocean for 20 days at a time. The purpose of this setup is to limit model drift, but at the same time allow the ocean to evolve without constraints. ROMS is a free-surface, hydrostatic primitive equation ocean circulation model. Horizontal resolution is 3.5×3.5 km ($1/32^\circ$ Mercator) with 50 sigma layers. We use the K-profile

parameterization (KPP) turbulence closure scheme (Large et al., 1994) in the surface and bottom boundary layer and Richardson number-dependent mixing in the ocean interior. The model is initialized from the HYbrid Coordinate Ocean Model (HYCOM) GLBa0.08 $1/12^\circ$ Navy Coupled Ocean Data Assimilation (NCODA) system (Metzger et al., 2014), and lateral boundary conditions are a radiation/nudging scheme with radiation on outflow and nudging on inflow to HYCOM/NCODA, with a three-day relaxation time scale (Marchesio et al., 2001). The vertical grid is 50 sigma layers, which in the absence of topography appears as depth coordinates in the upper ocean with levels at 0, 5, 10, 15, 25, 30, 40, 50 m, and so on. Flux forcing is computed using the model state and atmospheric state updated every three hours, with turbulent fluxes calculated using bulk formulae (Large and Pond, 1981). Tidal forcing is implemented through the open boundary conditions with semidiurnal (M_2 and S_2 constituents) and diurnal (O_1 and K_1 constituents) tidal velocities and sea level from TPXO7.2 (Egbert and Erofeeva, 2002). River discharge is from the Dai and Trenberth (2002) monthly river climatology. Horizontal tracer mixing is via a harmonic eddy viscosity coefficient of 2.0 m² s⁻¹ and momentum is via a harmonic eddy viscosity coefficient of 10.0 m² s⁻¹. A linear bottom drag of 3×10^{-4} m s⁻¹ and a nonlinear drag coefficient of 3×10^{-3} are used.

RESULTS

Enhanced Shear Generation at the Mixed Layer Base

Figure 2 presents an analysis of the data collected at the BD09 mooring from August to September 2013. The wind stress magnitude changes with time (Figure 2a,b) and excites inertial currents in the ML (Figure 2c). The MLD (red line; Figure 2b) corresponds closely with the wind stress magnitude (Figures 2a and 3a). MLD is defined as the depth at which density exceeds the surface value (here $z = 5$ m is the

shallowest measurement) by 0.03 kg m^{-3} . The mean MLD is 15 m and is modulated by the active-break spell of the summer monsoon winds. After August 28, the ML is relatively shallow with a MLD hovering around 5 m due to very fresh water at the ocean surface and the consequent strong salinity stratification (Figure 2d,e).

The MLD and the strength of stratification below the ML are important parameters that determine the extent to which the ML inertial currents can propagate into the deeper ocean. On August 6–7, the MLD approaches the depth of the stratification maximum (Figure 2e), which may be related to the downward NIW group propagation on August 9–11 below 40 m (note the upward phase propagation or wave crest orientation in time; Figure 2c).

In September, even when both ML inertial currents are large and the depth difference between the ML and the stratification maximum is small, it is difficult to relate bursts of near-inertial currents in the interior to surface currents. Much of the shear remains at the base of the ML.

To better understand the near-inertial motions, we examine the vertical structure of the base of the ML and the time evolution of shear there. This interface between the stratified interior and unstratified surface layer of the ocean is known as the transition layer (TL; Ferrari and Boccaletti, 2004; Johnston and Rudnick, 2009). We calculate the transition layer thickness (TLT) as the depth of the shear maximum (D) below the MLD: $\text{TLT} = D - \text{MLD}$. Similar calculations can

be made with the stratification maximum. Our estimates of TLT are 3–40 m, which are consistent with a previous study in the Arabian Sea (Majumder et al., 2015). Due to the wider vertical spacing of temperature and salinity measurements at the mooring, we use TLT based on shear for the rest of our calculations because the ADCP bin sizes are 5 m. The TL is the region between the seven-day low-passed lines in Figure 2f. On August 6–7, when the TL thins for two days (TLT is difference between MLD in gray, which in not low pass filtered, and the depth of the stratification maximum; Figure 2e), there is some downward near-inertial energy propagation. Otherwise, until August 15, the TL is thick and, despite some inertial motions in the ML, little energy

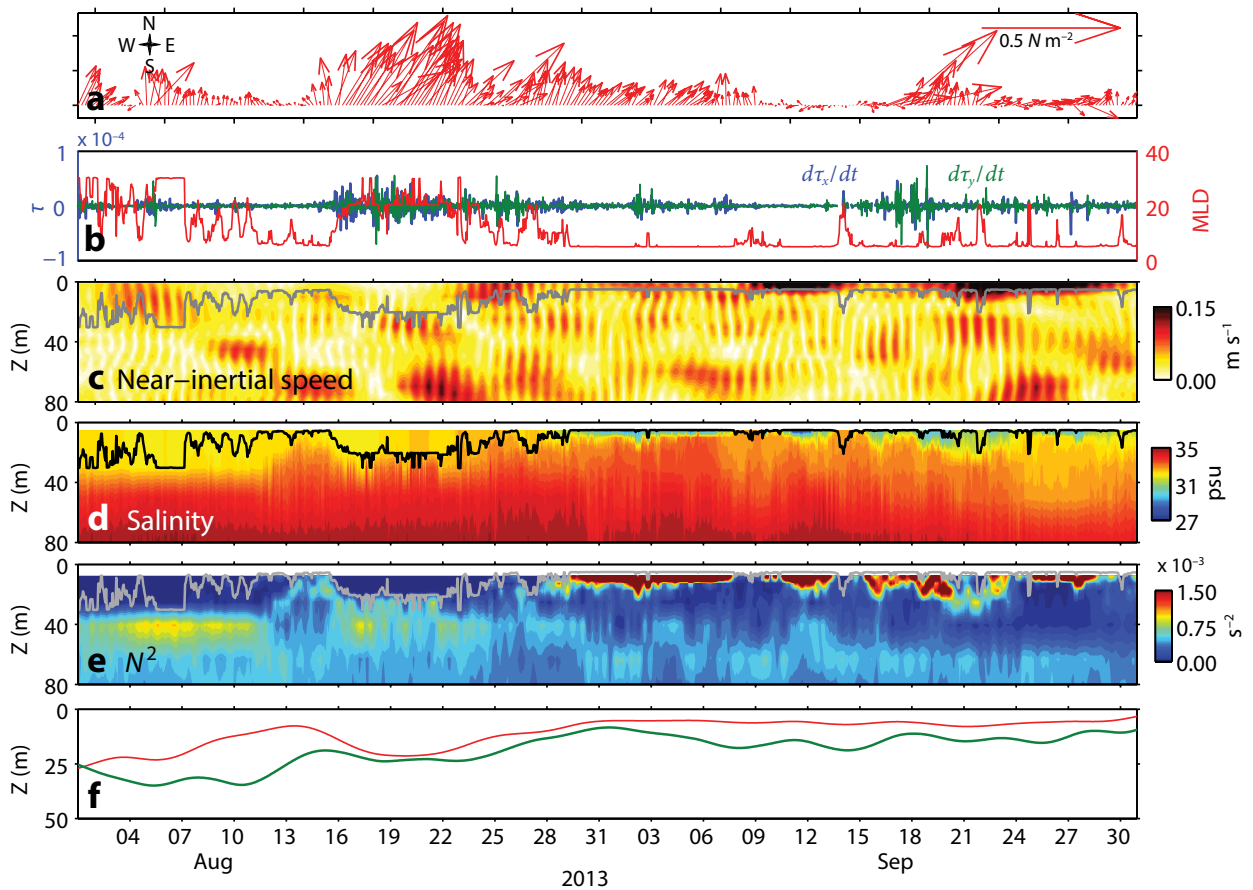


FIGURE 2. Analysis of the data obtained during August to September 2013 from OMNI mooring BD09. (a) Wind stress as a function of time (plotted as a vector with zonal and meridional components). (b) Temporal rate of change of zonal (blue) and meridional (green) components of wind stress as a function of time; the red curve shows the variation of the mixed layer depth with time. (c) Net magnitude of the near-inertial currents (obtained after filtering the zonal and meridional velocity components around the local inertial frequency) plotted as a function of time and depth. (d) Salinity plotted as a function of time and depth. (e) Square of the buoyancy frequency plotted as a function of time and depth. (f) Seven-day low-passed mixed layer depth (red) and maximum shear-squared depth (green). The gray curves in (c) and (e) and the black curve in (d) show the location of the bottom of the mixed layer.

propagates downward (Figure 2c). The TL acts as a barrier. After August 22, the stratification maximum near 40 m depth disappears and is replaced by the shallow stratification maximum due to fresher surface water (Figure 2e). Then, when wind changes excite ML near-inertial motions, there is downward propagation beneath the ML (Figure 2b,c). ML near-inertial motions decay in about three to seven days (Figure 2c).

For the idealized scenario of an infinitely deep ocean without background flow and with an abrupt jump in the stratification at the base of the ML from zero in the ML to a finite value in the ocean interior, Moehlis and Llewellyn-Smith (2001) gave an analytical estimate for the time scale over which the near-inertial energy in the ML decays via downward propagation of NIWs. Specifically, they calculate that over a time of T_d and $2T_d$, 50% and 82% of the ML energy is transferred to regions below the ML via downward propagation of NIWs. Here, T_d is given by $T_d = f^{1/3}(\beta^2 H^2 N^2)^{-1/3}$, where H is the MLD, and N^2 the uniform deep ocean stratification. Typical BoB values are: $f = 4.47 \times 10^{-5} \text{ s}^{-1}$,

$\beta = 2.17 \times 10^{-11} \text{ s}^{-1} \text{ m}^{-1}$, and $N = 0.02 \text{ s}^{-1}$. For MLDs of 10 and 50 m, $T_d = 31$ and 11 days, respectively, thus insufficiently explaining the decay time scales found in our measurements. We note, however, that either a sheared background flow or an equivalent β effect via the presence of mesoscale eddies can affect the decay time scales (see Introduction).

Next, the time evolution of bulk shear of the TL is estimated from the mooring data. We use a simple two-layer model of the upper ocean forced only by wind for the calculation (Brannigan et al., 2013; Majumder et al., 2015). The model approximates (1) the ML as a slab that accelerates due to wind and interfacial stress, and (2) the lower layer as quiescent. Given the observed wind stress, MLD, and the TLT, the model predicts current shear between the upper and lower layers. The shear is the velocity difference between the layers divided by the TLT. Shear generation is maximized (1) for thin ML and TL, and (2) when the wind stress, which varies relatively little in direction, aligns with the rotating inertial currents. Multiple events of mean bulk-shear-squared with amplitudes varying from

$0.1\text{--}2 \times 10^{-4} \text{ s}^{-2}$ are present during the summer monsoon in 2013 (Figure 3b). The shear magnitude increases in the presence of the thin freshwater layer during September. The shear generation term, $P(S^2)$, roughly follows the time evolution term ($\partial S^2/\partial t$; Figure 3c). When the phases of the bulk shear and the relative stress align, shear generation occurs ($0^\circ =$ direction of relative shear in Figure 3d). Note the main shear generation event is September 16–18 when this alignment occurs and is coincident with a wind event. Despite somewhat larger wind stresses in mid-August, the lack of alignment leads to little shear generation.

Since there are other sources of observed shear besides near-inertial currents, the time series are band passed around the inertial frequency (Figure 4). In the TL, there is little near-inertial shear in early August due to weaker winds and thicker TL. However, from late August onward, the ML shoals (Figure 2). ML inertial currents and near-inertial shear in the TL are elevated in four episodes centered on August 26 and September 3, 11, and 23 (Figures 2c and 4a). During and after the wind event on September 19 (Figure 2a),

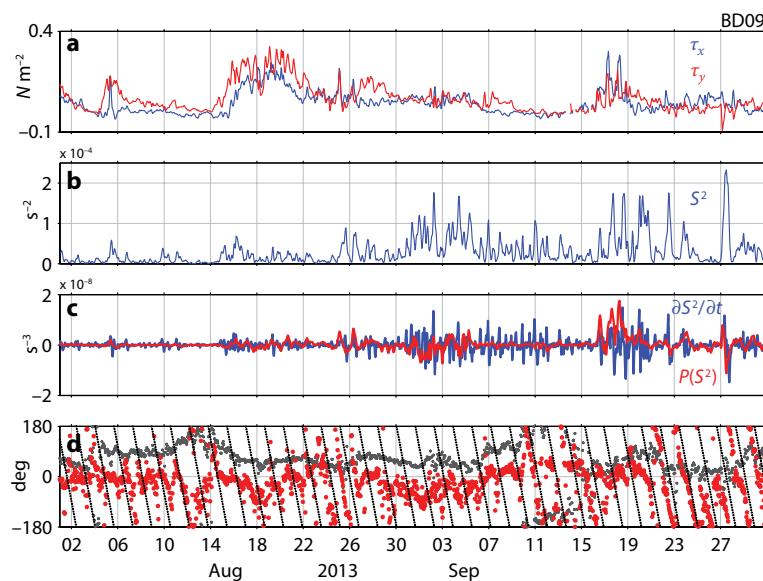


FIGURE 3. (a) Hourly zonal (τ_x ; red) and meridional (τ_y ; blue) wind stress from mooring BD09. (b) Two-hour low-pass-filtered shear-squared (S^2). (c) Two-hour low-pass-filtered shear-generation $P(S^2)$ (red) and time evolution $\partial S^2/\partial t$ (blue). (d) Direction of relative shear (black) and shear (red). Black solid lines denote local inertial rotation. All of the plots correspond to the period August 16 to September 30, 2013.

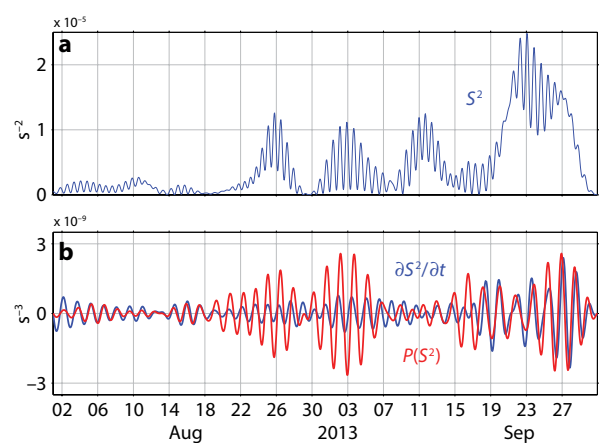


FIGURE 4. (a) Near-inertial shear in the transition layer is obtained by band passing the total shear (Figure 3b). (b) The near-inertial shear evolution (blue) and near-inertial shear generation (red) are in better agreement than the unfiltered terms in Figure 3c.

shear generation and time evolution agree well (Figure 4b). Agreement is also good under moderate winds from the beginning of the record until August 18. From August 16–23, the ML deepens under strong winds (Figure 2a,b), which indicates an energy sink for the shear that is being produced. From August 25 to September 7, shear generation is larger than shear evolution, which suggests energy is being supplied to NIWs and dissipating in the TL (Figure 4b). This is consistent with a thin ML and a TL thickening (August 31 to September 7; Figure 2f). These results, along with previous work by Brannigan et al. (2013) and Majumder et al. (2015), suggest this two-layer model is a useful tool for evaluating the near-inertial ML energy budget.

Rapid Downward NIW Propagation at a Front

The float was released from R/V *Revelle* at a freshwater front in the northern BoB and advected westward in a looping trajectory, which is a combination of mean

flow, semidiurnal tide (period is 0.5 day), and near-inertial oscillations (period is 1.7 days; Figures 1c and 5c). Here, we examine how these inertial motions decay in the surface ML and propagate downward into the ocean interior. Based on observations from this float and two other glider missions, clear and rapid downward propagation is found near fronts, where the distance between the ML and the stratified interior is reduced. Otherwise, when wind events occur, the inertial motions are concentrated in the near-surface fresh layer and do not cross the barrier layer beneath it.

On November 27, there is a sudden wind shift (Figure 5a). To determine the frequency content of the vector wind time series, we examine the scalogram obtained from the wavelet analysis. The scalogram is analogous to a power spectrum from Fourier analysis, but displays variance as a function of time and the oscillation's period (Figure 5b). Furthermore, a wavelet transform of the vector winds or currents

separately resolves counterclockwise and clockwise rotation. This particular wind shift projects onto a clockwise-rotating inertial signal from November 25–28 (Figure 5b). The magnitude of the inertial signal in the wind is about 1 m s^{-1} (blue line; Figure 5f), which is a fraction of the total wind speed of over 10 m s^{-1} (Figure 5a). Until November 25, 2013, the winds have a diurnal component, which weakens and then grows again on November 29 (Figure 5b).

Initially, the depth-mean current oscillations are semidiurnal (Figure 5c). Also on November 27, a distinct change to near-inertial oscillations in currents is visible without any filtering (Figure 5c). The vector components of the current are denoted u and v , which are positive eastward and northward. The near-inertial currents decay by a factor of two by December 4.

NIW currents rotate in the clockwise direction due to Earth's rotation. Thus, the wind shift's projection onto clockwise-rotating winds favors the

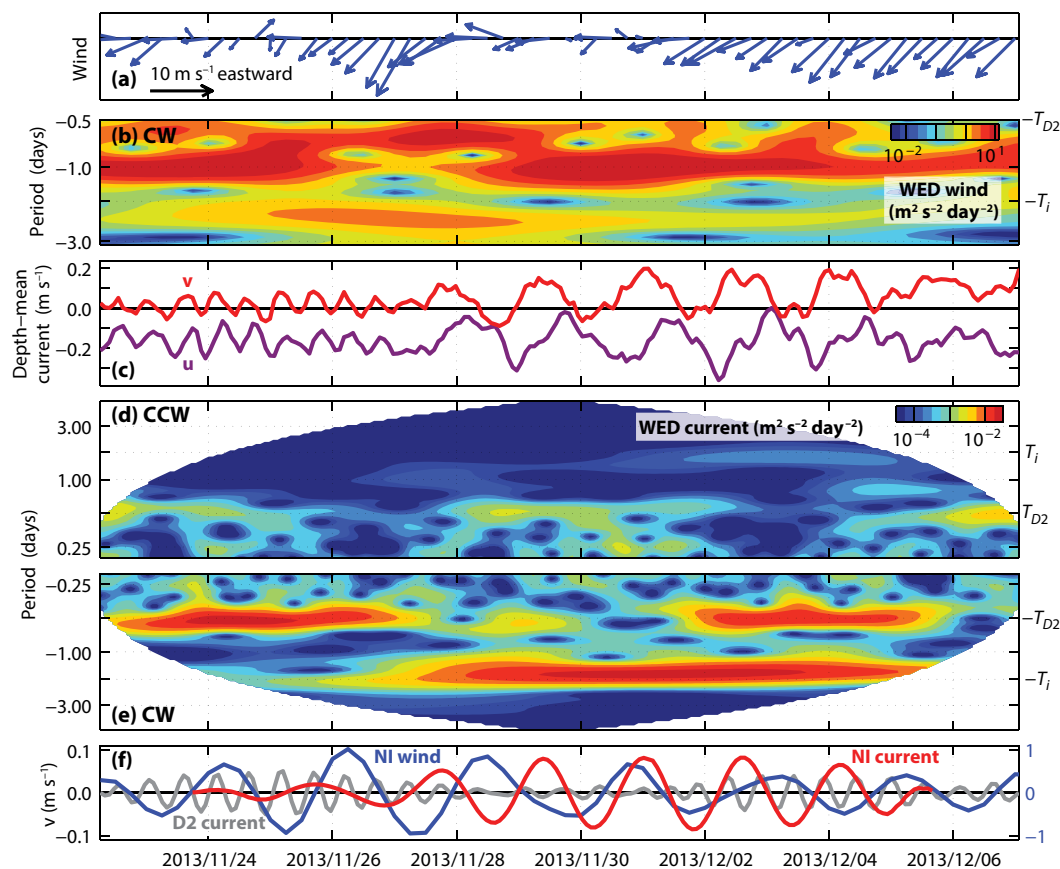


FIGURE 5. (a) Wind vectors show a sudden shift on November 27. (b) The shift projects onto a clockwise near-inertial rotation in a scalogram, which displays wind variance (or wavelet energy density, WED) as a function of time and oscillation period. T_i and T_{D2} denote the inertial and semidiurnal periods. (c) Depth-mean currents also show a shift from semidiurnal to near-inertial currents after the wind shift. (d) Current vector variance is shown in scalograms for counterclockwise and clockwise (e) rotation. Clockwise variance is dominant due to internal waves with a sudden onset of near-inertial currents on November 27. (f) Northward currents and winds are band passed within 25% of the semidiurnal and inertial frequencies (compare to Figure 5c). Gray, red, and blue lines indicate semidiurnal current, near-inertial current, and near-inertial wind, respectively.

excitation of clockwise currents. The currents and winds in the near-inertial and semidiurnal frequency bands are reconstructed from the wavelet transform by using wavelet coefficients from a pass band within 25% of each frequency. A near-inertial peak ($\omega = 1.1 f$) is found from November 28 to December 3 (Figure 5e,f).

Semidiurnal currents are initially present, abruptly disappear during the wind shift from November 27 to December 2, and then reappear (Figure 5e,f). The reason for the abrupt change in semidiurnal currents is unclear, but could be related to the effect of stratification on semidiurnal internal wave propagation, to the spring neap cycle, or to the position of the float with respect to the front.

The float encounters water on either side of the front multiple times due to surface-intensified inertial motions, which move surface waters more with respect to the float as it profiles to 250 m. With southward near-inertial currents on November 30 (Figure 5f), for example, the freshwater front is advected southward (Figure 6b), the mixed layer deepens (black line; Figure 6a) and becomes less stratified (Figure 6a), and denser water is moved over the float (Figure 6b). This description is qualitatively consistent with the model, where the observed

float trajectory is along a modeled freshwater front (Figure 1c).

Since the velocity measurements are a depth mean, we use near-inertial density fluctuations to understand the depth-dependent NIW propagation into the interior (Figure 6b–d). An example scalogram from 150 m depth has similar structure to that of the depth-mean currents—namely, semidiurnal fluctuations are interrupted on November 28 and resume two days later, and near-inertial fluctuations are maximum from November 30 to December 3 (Figure 6c). From similar scalograms, density fluctuations in the near-inertial frequency band are obtained from a wavelet band pass at each depth from the surface to 250 m. To visualize the fluctuations better, they are scaled by a factor mainly related to the stratification, and the plotted quantity is energy, once it is squared (Figure 6d).

The fluctuations are largest in the ML and then propagate downward reaching 250 m on December 2, which is within four to six days (or two to three inertial periods) of the wind shift. This downward energy propagation of about 30 m day^{-1} is rapid compared to other available measurements. The energy propagates downward in a group of several waves, which is expected for a forcing event of limited duration. A feature of internal waves with

downward energy or group propagation is that phase propagation is upward (i.e., wave crests slope upward with time). Also, these observations provide an estimate of the vertical wavelength of the waves in the interior. The wavelength changes with stratification, but on December 4 it appears to be greater than 200 m and probably around 300 m.

The internal wave dispersion relation relates wave frequency to other quantities, such as wavelength. We use the observed vertical wavelength and vertical group speed to establish limits for the horizontal wavelength (Figure 7) as follows. (1) The observed vertical group speed is 33 m day^{-1} , but lower and upper limits of 20 m day^{-1} and 40 m day^{-1} are not unreasonable (Figure 6d). (2) The observed vertical wavelength is over 200 m and likely at least 300 m (Figure 6d). (3) We use the observed frequencies from near-inertial velocity and density fluctuations as lower and upper limits on frequencies ($\omega = 1.1 f$ and $1.2 f$). Combining these three limits produces a range of possible consistent values (yellow stippled area, Figure 7). However, we emphasize that as the waves approach the inertial frequency and the horizontal wavelength increases, wave properties become increasingly sensitive to wave frequency. Based on a frequency of $1.1 f$, a vertical group velocity

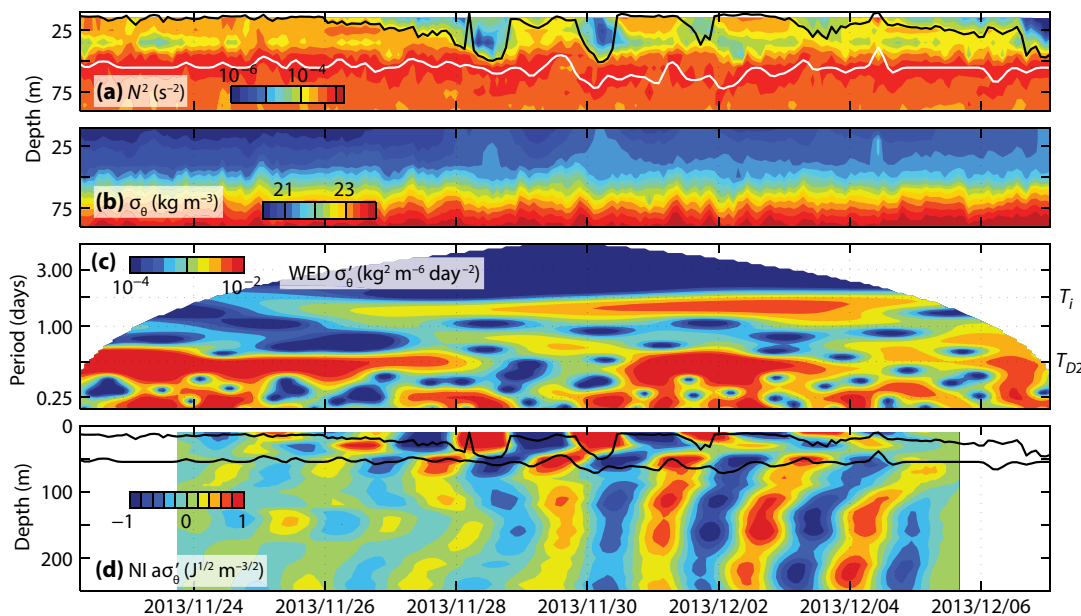


FIGURE 6. Since the float was released at a front, near-inertial oscillations move (a) less-stratified and (b) denser upper-ocean water from the north (i.e., southward current in Figure 5f) over the float as it profiles deeper. Panel (a) shows the mixed layer depth (black line) and the depth of maximum stratification (white line). (c) A scalogram shows variance in density fluctuations at semidiurnal and inertial periods. (d) Near-inertial density fluctuations from a band pass (within 25% of the inertial frequency as in Figure 5f) are scaled to equal potential energy when squared. Downward energy propagation to 250 m in six days is found, while mixed layer fluctuations decay.

of 33 m day^{-1} , and a vertical wavelength of 300 m, the horizontal wavelength is about 300 km. This value is comparable to the spacing of the adjacent cyclonic (clockwise) and anticyclonic (counterclockwise) eddies, which lie south and north of the float's trajectory (Figure 1c).

Mixed Layer Energy Decay Estimate

At the same time as the NIWs propagate downward in the interior ocean, the near-inertial density fluctuations in the ML decay substantially by December 4 (Figure 6d) as do the depth-mean currents (Figure 5c,f). Thus, the observed decay scale of the currents and density fluctuations is about seven days. Here, we estimate the ML energy removal by the downward-propagating NIW group.

First, the ML kinetic energy is estimated. The depth-mean currents over the float's dive profile are obtained from adjacent position fixes during surface intervals. However, since these currents are initiated by a sudden wind event, they are concentrated in the 10–50 m deep ML (black line denotes the MLD in Figure 6a and is from a 0.1 kg m^{-3} density difference from the surface). To estimate the near-inertial currents in the ML, we use the observed near-inertial depth-mean velocity (0.08 m s^{-1} , Figure 5f) and assume near-inertial fluctuations over the profiling range beneath the ML average to zero. For a 50 m deep ML, this yields an ML near-inertial current of 0.4 m s^{-1} . This corresponds to an ML kinetic energy of about 4 kJ m^{-2} . This value decreases if near-inertial fluctuations contribute to a non-zero depth-mean current over the profiling range.

Next, we estimate the downward energy flux. For this, we need the frequency of the NIWs seen in density fluctuations ($\omega = 1.2f$ from a wavelet analysis; Figure 6c), the kinetic to potential energy ratio of these waves at this frequency (about 6), and the observed potential energy (about 1 J m^{-3} ; Figure 6d). The downward energy flux is then estimated as 2.5 mW m^{-2} from the product of the

observed downward group velocity of 33 m day^{-1} and the total energy density of about 7 J m^{-3} , which is obtained from the sum of the observed potential energy and the estimated kinetic energy (potential energy times six, as noted above).

The ML energy decay time scale is estimated as the ML kinetic energy divided by the downward energy flux, yielding a value of about 19 days. We emphasize that this calculation is approximate, with large uncertainty, because (1) the depth-varying currents were not actually measured, and (2) the kinetic to potential energy ratio is especially sensitive to the wave frequency near the inertial frequency. If the frequency of the NIWs is instead $1.1f$ (as seen for the depth-mean currents; Figure 5e), then the kinetic to potential energy ratio almost doubles, the vertical energy flux estimate almost doubles, and the decay scale decreases to 11 days. Given the observed ML near-inertial decay scale of seven days, the downward-propagating NIW group may remove about half of the ML kinetic energy.

The remaining near-inertial energy may either propagate away as long-wavelength waves not detected by our methods or dissipate via turbulence in the highly sheared and stratified transition layer (region between black lines,

Figure 6d). The change of near-inertial density fluctuations with depth in the transition layer implies current shear of about 0.2 m s^{-1} over 10 m (or $S^2 = 4 \times 10^{-4} \text{ s}^{-2}$), which depends on the kinetic to potential energy ratio. Since the Richardson number is about 1 (N^2 in the transition layer is about 10^{-4} s^{-2} ; Figure 6a), this result suggests shear instability and turbulence are possible.

In summary, our interpretation of the data is that an impulsive wind event generates ML inertial motions, and a considerable fraction of the energy radiates rapidly downward in a group of short-wavelength NIWs near a density front. Some caveats are noted. The short vertical wavelength motions are likely well captured due to their slow horizontal propagation speeds, but waves with long vertical wavelengths have rapid horizontal propagation speeds and move rapidly out of the study area. On the other hand, long waves may propagate into the study area. Such waves could impact the ML near-inertial energy budget. No attempt has been made to identify such waves because of the float's limited profiling depth. However, the float traversed about 3° of longitude, moving with the depth-mean flow in the upper ocean, and does not provide a time series at a single point. This distance is comparable to the

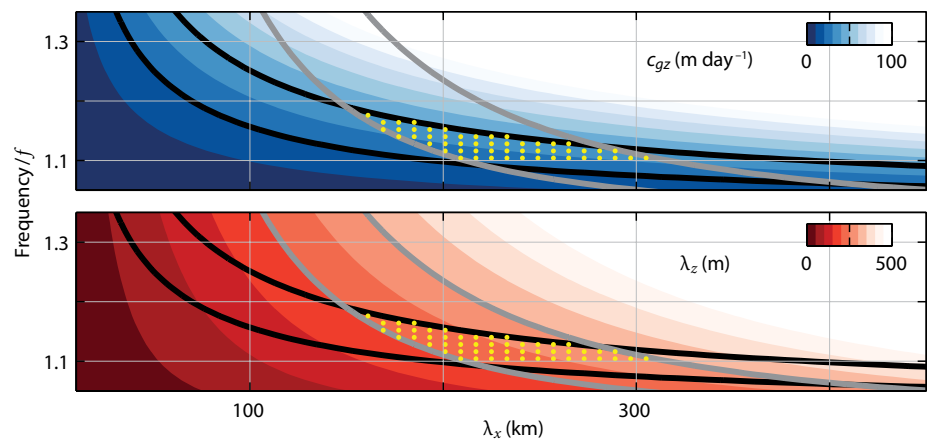


FIGURE 7. The internal wave dispersion relation is used to calculate the vertical (a) group velocity and (b) wavelength as functions of frequency and horizontal wavelengths. The horizontal wavelength is estimated by using observed limits on the vertical group velocity, the vertical wavelength, and the frequency—the yellow stippled area with frequencies of $1.1\text{--}1.2f$, group velocities of $20\text{--}40 \text{ m day}^{-1}$ (black lines), and vertical wavelengths of 200–300 m (gray lines).

estimated horizontal wavelength of the near-inertial waves but is much smaller than the scale of the atmospheric forcing. Thus, the float placement with respect to atmospheric forcing is not special. However, the float moved along a front sampling a coherent short-wavelength near-inertial signal.

SUMMARY

Shear at the base of the ML contributes to mixing, which affects the heat content and sea surface temperature of the ML and thus precipitation. Such effects may be more pronounced with a thin ML as in the BoB. Thus, how energy is removed from inertial motions, by either downward NIW energy propagation or shear generation at the base of the ML, is consequential.

Rapid downward propagation of short vertical wavelength NIW groups occurs near fronts, as observed by a float described here (and two additional glider missions, which were omitted for brevity). The NIW group propagates down to 200 m depth in about six days, yielding a vertical group speed of 30 m day^{-1} . The NIW vertical energy flux is sufficient to remove energy from the ML inertial motions in 11–19 days and is sensitive to the wave frequency. The observed ML inertial decay is about seven days, which suggests about half of the observed decay is due to the downward-propagating NIW group. No attempt has been made to estimate the contribution of waves with long wavelengths, which may radiate energy in the horizontal.

Elevated shear at the base of the ML likely dissipates some of the remaining energy through shear instability. Mooring data show shear generation is maximized beneath the ML in a two-layer model of the upper ocean, (1) when near-inertial currents align with the wind stress, and (2) for thin ML and transition layers. 

REFERENCES

- Alford, M.H., and M. Gregg. 2001. Near-inertial mixing: Modulation of shear, strain and microstructure at low latitude. *Journal of Geophysical Research* 106(C8):16, 947–16,968, <http://dx.doi.org/10.1029/2000JC000370>.
- Alford, M.H., J.A. MacKinnon, H.L. Simmons, and J.D. Nash. 2016. Near-inertial internal gravity waves in the ocean. *Annual Review of Marine Science* 8:95–123, <http://dx.doi.org/10.1146/annurev-marine-010814-015746>.
- Brannigan, L., Y.-D. Lenn, T.P. Rippeth, E. McDonagh, T.K. Chereskin, and J. Sprintall. 2013. Shear at the base of the oceanic mixed layer generated by wind shear alignment. *Journal of Physical Oceanography* 43(8):1,798–1,810, <http://dx.doi.org/10.1175/JPO-D-12-0104.1>.
- Chaigneau, A., O. Pizarro, and W. Rojas. 2008. Global climatology of near-inertial current characteristics from Lagrangian observations. *Geophysical Research Letters* 35, L13603, <http://dx.doi.org/10.1029/2008GL034060>.
- Chowdary, J.S., A. Parekh, S. Ojha, C. Gnanaseelan, and R. Kakatkar. 2016a. Impact of upper ocean processes and air-sea fluxes on seasonal SST biases over the tropical Indian Ocean in the NCEP Climate Forecasting System. *International Journal of Climatology* 36(1):188–207, <http://dx.doi.org/10.1002/joc.4336>.
- Chowdary, J.S., G. Srinivas, T.S. Fousiya, A. Parekh, C. Gnanaseelan, H. Seo, and J.A. MacKinnon. 2016. Representation of Bay of Bengal upper-ocean salinity in general circulation models. *Oceanography* 29(2):38–49, <http://dx.doi.org/10.5670/oceanog.2016.37>.
- Dai, A., and K.E. Trenberth. 2002. Estimates of freshwater discharge from continents: Latitudinal and seasonal variations. *Journal of Hydrometeorology* 2:660–687, [http://dx.doi.org/10.1175/1525-7541\(2002\)003<0660:EOFDFC>2.0.CO;2](http://dx.doi.org/10.1175/1525-7541(2002)003<0660:EOFDFC>2.0.CO;2).
- D'Asaro, E.A., C.C. Eriksen, M.D. Levine, P. Niiler, C.A. Paulson, and P. Van Meurs. 1995. Upper-ocean inertial currents forced by a strong storm: Part I. Data and comparisons with linear theory. *Journal of Physical Oceanography* 25:2,909–2,936, [http://dx.doi.org/10.1175/1520-0485\(1995\)025<2909:UOICFB>2.0.CO;2](http://dx.doi.org/10.1175/1520-0485(1995)025<2909:UOICFB>2.0.CO;2).
- Davis, R.E., J.T. Sherman, and J. Dufour. 2001. Profiling ALACEs and other advances in autonomous subsurface floats. *Journal of Atmospheric and Oceanic Technology* 18(6):982–993, [http://dx.doi.org/10.1175/1520-0426\(2001\)018<0982:PAOAI>2.0.CO;2](http://dx.doi.org/10.1175/1520-0426(2001)018<0982:PAOAI>2.0.CO;2).
- Dohan, K., and R. Davis. 2011. Mixing in the transition layer during two storm events. *Journal of Physical Oceanography* 41:42–66, <http://dx.doi.org/10.1175/2010JPO4253.1>.
- Egbert, G., and S. Erofeeva. 2002. Efficient inverse modeling of barotropic ocean tides. *Journal of Atmospheric and Oceanic Technology* 19(2):183–204, [http://dx.doi.org/10.1175/1520-0426\(2002\)019<0183:EIMOBO>2.0.CO;2](http://dx.doi.org/10.1175/1520-0426(2002)019<0183:EIMOBO>2.0.CO;2).
- Ekman, V.W. 1905. On the influence of the Earth's rotation on ocean-currents. *Arkiv för matematik, astronomi och fysik* 2(11):1–52.
- Elipot, S., R. Lumpkin, and G. Prieto. 2010. Modification of inertial oscillations by the meso-scale eddy field. *Journal of Geophysical Research* 115, C09010, <http://dx.doi.org/10.1029/2009JC005679>.
- Ferrari, R., and G. Boccaletti. 2004. Eddy-mixed layer interactions in the ocean. *Oceanography* 17(3):12–21, <http://dx.doi.org/10.5670/oceanog.2004.26>.
- Fousiya, T., A. Parekh, and C. Gnanaseelan. 2015. Interannual variability of upper ocean stratification in Bay of Bengal: Observational and modeling aspects. *Theoretical and Applied Climatology* 1–17, <http://dx.doi.org/10.1007/s00704-015-1574-z>.
- Gill, A.E. 1982. *Atmosphere-Ocean Dynamics*. Academic Press, 662 pp.
- Gill, A.E. 1984. On the behavior of internal waves in the wake of a storm. *Journal of Physical Oceanography* 14:1,129–1,151, [http://dx.doi.org/10.1175/1520-0485\(1984\)014<1129:OTBOIW>2.0.CO;2](http://dx.doi.org/10.1175/1520-0485(1984)014<1129:OTBOIW>2.0.CO;2).
- Gordon, A.L., E.L. Shroyer, A. Mahadevan, D. Sengupta, and M. Freilich. 2016. Bay of Bengal: 2013 northeast monsoon upper-ocean circulation. *Oceanography* 29(2):82–91, <http://dx.doi.org/10.5670/oceanog.2016.41>.
- Goswami, B.N., S.A. Rao, D. Sengupta, and S. Chakravorty. 2016. Monsoons to mixing in the Bay of Bengal: Multiscale air-sea interactions and monsoon predictability. *Oceanography* 29(2):18–27, <http://dx.doi.org/10.5670/oceanog.2016.35>.
- Hebert, H., and J. Moum. 1994. Decay of a near-inertial wave. *Journal of Physical Oceanography* 24(11):2,334–2,351, [http://dx.doi.org/10.1175/1520-0485\(1994\)024<2334:DOANIW>2.0.CO;2](http://dx.doi.org/10.1175/1520-0485(1994)024<2334:DOANIW>2.0.CO;2).
- Hormann, V., L.R. Centurioni, A. Mahadevan, S. Essink, E.A. D'Asaro, and B. Praveen Kumar. 2016. Variability of near-surface circulation and sea surface salinity observed from Lagrangian drifters in the northern Bay of Bengal during the waning 2015 southwest monsoon. *Oceanography* 29(2):124–133, <http://dx.doi.org/10.5670/oceanog.2016.45>.
- Jochum, M., B.P. Briegleb, G. Danabasoglu, W.G. Large, N.J. Norton, S.R. Jayne, M.H. Alford, and F.O. Bryan. 2013. The impact of oceanic near-inertial waves on climate. *Journal of Climate* 26(9):2,833–2,844, <http://dx.doi.org/10.1175/JCLI-D-12-00181.1>.
- Johnston, T.M.S., and D.L. Rudnick. 2009. Observations of the transition layer. *Journal of Physical Oceanography* 39:780–797, <http://dx.doi.org/10.1175/2008JPO3824.1>.
- Johnston, T.M.S., D.L. Rudnick, and S.M. Kelly. 2015. Standing internal tides in the Tasman Sea observed by gliders. *Journal of Physical Oceanography* 45(11):2,715–2,737, <http://dx.doi.org/10.1175/JPO-D-15-0038.1>.
- Johnston, T.M.S., D.L. Rudnick, and E. Pallàs-Sanz. 2011. Elevated mixing at a front. *Journal of Geophysical Research* 116, C11033, <http://dx.doi.org/10.1029/2011JC007192>.
- Kalnay, E.M., M. Kanamitsu, R. Kistler, W. Collins, D. Deaven, L. Gandin, M. Iredell, S. Saha, G. White, J. Woollen, and others. 1996. The NCEP/NCAR 40-year reanalysis project. *Bulletin of the American Meteorological Society* 77:437–471, [http://dx.doi.org/10.1175/1520-0477\(1996\)077<0437:TNYRP>2.0.CO;2](http://dx.doi.org/10.1175/1520-0477(1996)077<0437:TNYRP>2.0.CO;2).
- Kunze, E. 1985. Near-inertial wave propagation in geostrophic shear. *Journal of Physical Oceanography* 15:544–565, [http://dx.doi.org/10.1175/1520-0485\(1985\)015<0544:NIWPWG>2.0.CO;2](http://dx.doi.org/10.1175/1520-0485(1985)015<0544:NIWPWG>2.0.CO;2).
- Large, W.G., J.C. McWilliams, and S.C. Doney. 1994. Oceanic vertical mixing: A review and model with a nonlocal boundary layer parameterization. *Reviews of Geophysics* 32:363–403, <http://dx.doi.org/10.1029/94RG01872>.
- Large, W. G., and S. Pond. 1981. Open ocean momentum flux measurements in moderate to strong winds. *Journal of Physical Oceanography* 11:324–336.
- Lucas, A.J., J.D. Nash, R. Pinkel, J.A. MacKinnon, A. Tandon, A. Mahadevan, M.M. Omand, M. Freilich, D. Sengupta, M. Ravichandran, and A. Le Boyer. 2016. Adrift upon a salinity-stratified sea: A view of upper-ocean processes in the Bay of Bengal during the southwest monsoon. *Oceanography* 29(2):134–145, <http://dx.doi.org/10.5670/oceanog.2016.46>.
- MacKinnon, J.A., J.D. Nash, M.H. Alford, A.J. Lucas, J.B. Mickett, E.L. Shroyer, A.F. Waterhouse, A. Tandon, D. Sengupta, A. Mahadevan,

- and others. 2016. A tale of two spicy seas. *Oceanography* 29(2):50–61, <http://dx.doi.org/10.5670/oceanog.2016.38>.
- Majumder, S., A. Tandon, D.L. Rudnick, and J.T. Farrar. 2015. Near-inertial kinetic energy budget of the mixed layer and shear evolution in the transition layer in the Arabian Sea during the monsoons. *Journal of Geophysical Research* 120(9):6,492–6,507, <http://dx.doi.org/10.1002/2014JC010198>.
- Marchesiello, P., J.C. McWilliams, and A. Shchepetkin. 2001. Open boundary conditions for long-term integration of regional oceanic models. *Ocean Modelling* 3:1–20, [http://dx.doi.org/10.1016/S1463-5003\(00\)00013-5](http://dx.doi.org/10.1016/S1463-5003(00)00013-5).
- Metzger, E.J., O.M. Smedstad, P.G. Thoppil, H.E. Hurlburt, J.A. Cummings, A.J. Wallcraft, L. Zamudio, D.S. Franklin, P.G. Posey, M.W. Phelps, and others. 2014. US Navy Operational Global Ocean and Arctic Ice Prediction Systems. *Oceanography* 27(3):32–43, <http://dx.doi.org/10.5670/oceanog.2014.66>.
- Moehlis, J., and S.G. Llewellyn-Smith. 2001. Radiation of mixed layer near-inertial oscillations into the ocean interior. *Journal of Physical Oceanography* 31:1,550–1,560, [http://dx.doi.org/10.1175/1520-0485\(2001\)031<1550:ROMLNI>2.0.CO;2](http://dx.doi.org/10.1175/1520-0485(2001)031<1550:ROMLNI>2.0.CO;2).
- Munk, W. 1981. Internal waves and small scale processes. Pp. 264–291 in *Evolution of Physical Oceanography*. B. Warren, and C. Wunsch, eds, The MIT Press.
- Parekh, A., J.S. Chowdary, O. Sayantani, and T.S. Fousiya. 2015. Tropical Indian Ocean surface salinity bias in Climate Forecasting System coupled models and the role of upper ocean processes. *Climate Dynamics* 46:2,403–2,422, <http://dx.doi.org/10.1007/s00382-015-2709-8>.
- Park, J.J., K. Kim, and R.W. Schmitt. 2009. Global distribution of the decay timescale of mixed layer inertial motions observed by satellite-tracked drifters. *Journal of Geophysical Research* 114, C11010, <http://dx.doi.org/10.1029/2008JC005216>.
- Plueddemann, A.J., and J.T. Farrar. 2006. Observations and models of the energy flux to mixed-layer inertial currents. *Deep Sea Research Part II* 53:5–30, <http://dx.doi.org/10.1016/j.dsr2.2005.10.017>.
- Rudnick, D.L., and S.T. Cole. 2011. On sampling the ocean using underwater gliders. *Journal of Geophysical Research* 116, C08010, <http://dx.doi.org/10.1029/2010JC006849>.
- Sarkar, S., H.T. Pham, S. Ramachandran, J.D. Nash, A. Tandon, J. Buckley, A.A. Lotliker, and M.M. Omand. 2016. The interplay between submesoscale instabilities and turbulence in the surface layer of the Bay of Bengal. *Oceanography* 29(2):146–157, <http://dx.doi.org/10.5670/oceanog.2016.47>.
- Sarma, V.V.S.S., G.D. Rao, R. Viswanadham, C.K. Sherin, J. Salisbury, M.M. Omand, A. Mahadevan, V.S.N. Murty, E.L. Shroyer, M. Baumgartner, and K.M. Stafford. 2016. Effects of freshwater stratification on nutrients, dissolved oxygen, and phytoplankton in the Bay of Bengal. *Oceanography* 29(2):222–231, <http://dx.doi.org/10.5670/oceanog.2016.54>.
- Shroyer, E.L., D.L. Rudnick, J.T. Farrar, B. Lim, S.K. Venayagamoorthy, L.C. St. Laurent, A. Garanaik, and J.N. Moum. 2016. Modification of upper-ocean temperature structure by subsurface mixing in the presence of strong salinity stratification. *Oceanography* 29(2):62–71, <http://dx.doi.org/10.5670/oceanog.2016.39>.
- Simmons, H.L., and M.H. Alford. 2012. Simulating the long-range swell of internal waves generated by ocean storms. *Oceanography* 25(2):30–41, <http://dx.doi.org/10.5670/oceanog.2012.39>.
- Tandon, A., E.A. D'Asaro, K.M. Stafford, D. Sengupta, M. Ravichandran, M. Baumgartner, R. Venkatesan, and T. Paluszkiwicz. 2016. Technological advancements in observing the upper ocean in the Bay of Bengal: Education and capacity building. *Oceanography* 29(2):242–253, <http://dx.doi.org/10.5670/oceanog.2016.56>.
- Thangaprakash, V.P., M.S. Girishkumar, K. Suprit, N. Suresh Kumar, D. Chaudhuri, K. Dinesh, A. Kumar, S. Shivaprasad, M. Ravichandran, J.T. Farrar, and others. 2016. What controls seasonal evolution of sea surface temperature in the Bay of Bengal? Mixed layer heat budget analysis using moored buoy observations along 90°E. *Oceanography* 29(2):202–213, <http://dx.doi.org/10.5670/oceanog.2016.52>.
- Venkatesan, R., V.R. Shamji, G. Latha, S. Mathew, R. Rao, A. Muthiah, and M. Atmanand. 2013. In situ ocean subsurface time-series measurements from OMNI buoy network in the Bay of Bengal. *Current Science* 104(9):1,166–1,177.
- Weller, R.A. 1982. The relation of near-inertial motions observed in the mixed layer during the JASIN (1978) experiment to the local wind stress and to the quasi-geostrophic flow field. *Journal of Physical Oceanography* 12:1,122–1,136, [http://dx.doi.org/10.1175/1520-0485\(1982\)012<1122:TRONIM>2.0.CO;2](http://dx.doi.org/10.1175/1520-0485(1982)012<1122:TRONIM>2.0.CO;2).
- Weller, R.A., S. Majumder, and A. Tandon. 2014. Diurnal restratification events in the southeast Pacific trade wind regime. *Journal of Physical Oceanography* 44(9):2,569–2,587, <http://dx.doi.org/10.1175/JPO-D-14-00261>.
- Wijesekera, H.W., E. Shroyer, A. Tandon, M. Ravichandran, D. Sengupta, P. Jinadas, H.J.S. Fernando, N. Agrawal, K. Arulanathan, G.S. Bhat, and others. In press. ASIRI: An Ocean-Atmosphere Initiative for Bay of Bengal. *Bulletin of the American Meteorological Society*, <http://dx.doi.org/10.1175/BAMS-D-14-00197.1>.
- Young, W.R., and M. Ben Jelloul. 1997. Propagation of near-inertial oscillations through ageostrophic flow. *Journal of Marine Research* 55:735–766, <http://dx.doi.org/10.1357/0022240973224283>.
- graduate student at the Centre for Atmospheric and Oceanic Sciences, Indian Institute of Science, Bangalore, India. **Manikandan Mathur** is Assistant Professor, Department of Aerospace Engineering, Indian Institute of Technology, Chennai, India. **Daniel L. Rudnick** is Professor, Scripps Institution of Oceanography, University of California, San Diego, La Jolla, CA, USA. **Debasis Sengupta** is Professor, Centre for Atmospheric and Oceanic Sciences, Indian Institute of Science, Bangalore, India. **Harper L. Simmons** is Associate Professor, School of Fisheries and Ocean Sciences, University of Alaska Fairbanks, Fairbanks, AK, USA. **Amit Tandon** is Professor of Mechanical Engineering, University of Massachusetts Dartmouth, North Dartmouth, MA, USA. **R. Venkatesan** is Group Head, Ocean Observations, National Institute of Ocean Technology, Chennai, India.

ARTICLE CITATION

Johnston, T.M.S., D. Chaudhuri, M. Mathur, D.L. Rudnick, D. Sengupta, H.L. Simmons, A. Tandon, and R. Venkatesan. 2016. Decay mechanisms of near-inertial mixed layer oscillations in the Bay of Bengal. *Oceanography* 29(2):180–191, <http://dx.doi.org/10.5670/oceanog.2016.50>.

ACKNOWLEDGMENTS

We are grateful to the masters, crews, and scientists on R/V *Roger Revelle* and ORV *Sagar Nidhi* for their help in carrying out the field program; to colleagues in the ASIRI and OMM programs for their collaboration; and to India's Ministry of Earth Sciences and the US Office of Naval Research for funding this work. The Instrument Development Group at the Scripps Institution of Oceanography designed and prepared the SOLO-II float. HYCOM NCODA data was used to initialize and provide boundary conditions for the regional ROMS runs reported here. The ROMS simulation was performed on the high-performance computing cluster of the Research Computing Systems at the University of Alaska Fairbanks Geophysical Institute. Funding for the development of HYCOM has been provided by the National Ocean Partnership Program and the Office of Naval Research. Data assimilative products using HYCOM are funded by the US Navy. Computer time for HYCOM was made available by the Department of Defense High Performance Computing Modernization Program. The output is publicly available at <http://hycom.org>. NCEP reanalysis data was provided by NOAA/OAR/ESRL PSD, Boulder, Colorado, USA. We thank two anonymous reviewers for their helpful comments.

AUTHORS

T.M. Shaun Johnston (shaunj@ucsd.edu) is Associate Research Oceanographer, Scripps Institution of Oceanography, University of California, San Diego, La Jolla, CA, USA. **Dipanjana Chaudhuri** is a